

Comparison of different imaging models handling partial coherence for aberration-corrected HRTEM at 40–80 kV

Z. Lee*, T. Lehnert, U. Kaiser, H. Rose

University of Ulm, Ulm, 89081, Germany



ARTICLE INFO

Keywords:

HRTEM
Incoherent summation
Envelope functions
Quasi-coherent
Transmission cross-coefficient
 C_s -Corrected
 C_c/C_s -Corrected

ABSTRACT

Partial coherence of the electron waves leaving the specimen is taken into account in the high-resolution transmission electron microscopy (HRTEM) image simulation by mainly three methods - the incoherent summation approach, the transmission cross-coefficient (TCC) model, and the quasi-coherent model. In the incoherent summation approach, coherent images are calculated for each point in the effective source and summed up incoherently. The TCC is the transfer function of the microscope obtained based on the incoherent summation approach. An analytical form of the TCC can be derived by assuming a Gaussian distribution for the source radiation and for the variation of the focal length caused by the energy spread of the effective source. In the quasi-coherent model, the partial coherence effect is simplified by multiplying the wave function at the diffraction plane with the envelope functions. Envelope functions suppress the contributions to the image contrast from waves which do not propagate along the optical axis. The quasi-coherent model is usually sufficient for the image simulation of weak phase objects. This model is more computationally efficient than both the incoherent summation approach and the TCC model. For the C_s -corrected and C_c/C_s -corrected microscopes operating at 80 kV, we have compared images simulated by using the three models with the experimental images. The comparison shows that the quasi-coherent model also provides a sufficient approximation for the image simulation of high-Z materials if chromatic aberration is corrected and the samples comprise only several atomic layers. In the case of only C_s -correction, the incoherent summation approach or the TCC model needs to be employed for modelling the imaging of high-Z samples even though it is more computationally consuming.

1. Introduction

A reliable interpretation of the experimental high-resolution transmission electron microscopy (HRTEM) image contrast requires quantitative comparison between the experiments and simulations. A well-accepted method is the incoherent summation approach [1–5]. In this approach, the interaction between the sample and the incident electron wave emitting from each point in the effective source is usually modelled by a multislice algorithm, and the propagation of the outgoing waves is described by a convolution between the waves and the transfer function determined by the geometric aberrations. Coherent images simulated for each point in the effective source are then summed up incoherently. Representative applications which provide the possibility to calculate images using the incoherent summation approach are QSTEM developed by Koch [6] and STEM SIM developed by Rosenauer [7].

The transmission cross-coefficient (TCC) is the transfer function of the microscope obtained from the incoherent summation approach. The analytical form of the TCC can be derived by assuming a Gaussian

distribution for the source radiation and for the variation of focal length caused by the energy spread of the source [8–11]. The first-order TCC is derived by considering only linear terms from the Taylor expansion of the microscope aberrations [8–10]. An improved TCC includes also the high-order terms but has a complicated form [10,11]. Applications which allow image simulation using the TCC include xHREM developed by Ishizuka [12], JEMS developed by Stadelmann [13], STEM SIM developed by Rosenauer [7] and Dr. Probe developed by Bathel [14]. In order to improve the computational efficiency of the TCC model, Stadelmann suggested only including reflections in the reciprocal space with an amplitude larger than a self-defined threshold, which depends on the requirement of the accuracy [13].

In the quasi-coherent model, the propagation of the outgoing waves is described by a convolution between the waves and the contrast transfer function (CTF), which includes the geometric aberrations and envelope functions. Envelope functions account for the finite lateral coherence [9,10,15,16] and temporal coherence [9,10,16] of the source, as well as the instabilities of the microscope. The implementation of envelope functions indicates that the image intensity

* Corresponding author.

<https://doi.org/10.1016/j.ultramic.2019.01.007>

Received 6 September 2018; Received in revised form 7 January 2019; Accepted 21 January 2019

Available online 10 February 2019

0304-3991/ © 2019 Elsevier B.V. All rights reserved.

contributed by high spatial frequencies is suppressed or eliminated, especially in the case of the large-angle scattering of strong objects. The quasi-coherent model provides a sufficient approximation to model the imaging of weak-phase objects. In this case, the image intensity is dominantly contributed by the unscattered wave. Most standard applications provide the function of image simulation using the quasi-coherent model [6,7,13,14,17–19].

For an image represented by a $N \times N$ matrix, the number of arithmetic operations is in the order of $O(N^2 \log_2 N)$ for image simulations using the quasi-coherent model and is in the order of $O(N^4)$ for image simulations using the TCC model [3]. For an image simulation using the incoherent summation approach, the number of operations is in the order of $O(M_f M_s N^2 \log_2 N)$ with M_f and M_s denoting the number of points sampling the focal variation and the source radiation, respectively [3].

Due to the realization in the correction of the primary chromatic and geometric aberrations, sub-Angstrom resolution has been achieved at 40 kV for the SALVE microscope [20]. For C_c/C_s -corrected microscopes, the partial temporal coherence does not affect the image quality. However, other factors, in particular image spread caused by Johnson noise [21] and a residual focal spread [22], caused by the instability of the microscope elements, cannot be neglected. Therefore, it is necessary to incorporate also these factors into the image simulation program for C_c/C_s -corrected microscopes.

In our work, we have examined the validity of the first-order TCC for the simulation of aberration-corrected microscopy images, and compared images simulated by using the incoherent summation approach, the first-order TCC model, and the quasi-coherent model with the experiments. Comparisons have been made for both C_s -corrected and C_c/C_s -corrected microscopes operating at 80 kV. The influence of sample thickness, accelerating voltage and atomic number on the performance of the imaging models is discussed.

2. HRTEM image simulation in the case of partial coherence

Partial coherence refers to waves, which originate from different points of the effective source whose diameter is small compared to the focal length of the gun lens. Partial coherence is treated ‘incoherently’ in the HRTEM image simulation. This procedure first calculates the image intensity formed by the wave emanating from each point of the effective source. Because each point of this source radiates at random, the image intensities produced by the individual source points must be added.

The TCC is derived by incoherently summing up the transfer functions for each point of the effective source. The complete transfer function for HRTEM adopts the form [9]:

$$T(\vec{q}_1, \vec{q}_2) = \iint A(\vec{q}_1)A(\vec{q}_2)f(\epsilon)s(\vec{\Theta})\exp[-i\chi(\vec{q}_1 + k_0\vec{\Theta}, \Delta f + \epsilon)] \exp[i\chi(\vec{q}_2 + k_0\vec{\Theta}, \Delta f + \epsilon)]d\epsilon d^2\vec{\Theta}. \quad (1)$$

Here \vec{q}_1 and \vec{q}_2 are two-dimensional spatial frequency vectors, Δf is the mean defocus, A denotes the aperture function, χ is the aberration phase function, $\lambda = 2\pi/k_0$ is the wavelength of the incident wave, $s(\vec{\Theta})$ is the radiation function of the source, $f(\epsilon)$ is the function accounting for the focus variation.

The intensity distribution of a HRTEM image is given by

$$I(\vec{r}) = \iint \tilde{\psi}(\vec{q}_1)\tilde{\psi}^*(\vec{q}_2)T(\vec{q}_1, \vec{q}_2)e^{i2\pi\vec{r}(\vec{q}_1 - \vec{q}_2)}d^2\vec{q}_1d^2\vec{q}_2. \quad (2)$$

Here $\tilde{\psi}(\vec{q}_1)$ and $\tilde{\psi}^*(\vec{q}_2)$ are conjugated Fourier transforms of the exit-wave resulting from the illumination along the optical axis. In the case of beam tilt with a small angle θ , a shift vector $\vec{\tau} = \vec{\theta}/\lambda$ should be introduced. As a result, $\tilde{\psi}(\vec{q}_1)$ and $\tilde{\psi}^*(\vec{q}_2)$ in (2) are replaced by $\tilde{\psi}(\vec{q}_1 - \vec{\tau})$ and $\tilde{\psi}^*(\vec{q}_2 - \vec{\tau})$, respectively. In the case of large-angle beam tilt, a new exit-wave should be calculated for the corresponding tilting angle.

By replacing $T(\vec{q}_1, \vec{q}_2)$ in (2) with (1), one needs to calculate four

integrals to obtain a HRTEM image. The difference between the incoherent summation approach and the TCC model lies in the order of integration. For an incoherent summation approach, the integral pertaining to \vec{q}_1 or \vec{q}_2 is first calculated. The two integrals are conjugate, and their product is the image intensity formed by the wave emitting from one point of the effective source. The integrals pertaining to ϵ and $\vec{\Theta}$ are calculated subsequently, which corresponds to summing up the images contributed by different points of the effective source. The incoherent summation procedure is written as

$$I(\vec{r}) = \iint f(\epsilon)s(\vec{\Theta}) \left| \int \tilde{\psi}(\vec{q})A(\vec{q})\exp[-i\chi(\vec{q} + k_0\vec{\Theta}, \Delta f + \epsilon)]e^{i2\pi\vec{r}\vec{q}}d^2\vec{q} \right|^2 d\epsilon d^2\vec{\Theta}. \quad (3)$$

For the TCC model, the integrals pertaining to ϵ and $\vec{\Theta}$ are first calculated as in (1), followed by the 4D Fourier transform in (2). The calculation of a 4D Fourier transform is not computationally efficient. Fortunately, the 4D Fourier transform in (2) can be calculated in two steps. In the first step, one substitutes $\vec{q}_1 - \vec{q}$ for \vec{q}_2 in (2), giving the two-dimensional diffractogram:

$$\tilde{I}(\vec{q}) = \int \tilde{\psi}(\vec{q}_1)\tilde{\psi}^*(\vec{q}_1 - \vec{q})T(\vec{q}_1, \vec{q}_1 - \vec{q})d^2\vec{q}_1. \quad (4)$$

The time required for computing this integral increases with the size of the diffractogram $I(\vec{q})$. In the second step, the image intensity $I_D(\vec{r})$ is calculated by taking the Fourier transform of the diffractogram $I(\vec{q})$. The influence of the camera is also included by multiplying a modulation transfer function (MTF) with the diffractogram [23]:

$$I_D(\vec{r}) = \int \tilde{I}(\vec{q})MTF(\vec{q})e^{i2\pi\vec{r}\vec{q}}d^2\vec{q}. \quad (5)$$

2.1. Is the first-order TCC sufficient for the simulation of aberration-corrected HRTEM images at low voltages?

The first-order TCC is derived by assuming a Gaussian distribution for $s(\vec{\Theta})$ and $f(\epsilon)$ in (1), as well as by replacing the aberration function χ with the linear terms from its Taylor expansion [9,11]. An improved TCC is proposed by keeping χ in its original form and by including the spherically symmetric aberrations up to the third order [11]. The improved TCC has a much more complicated form compared with the first-order TCC.

Bonevich and Marks have pointed out in [11] that it is important to apply the improved form of TCC for the simulation of uncorrected microscopy images, exemplified by the case of the microscope operating at an accelerating voltage of 300 kV, with a beam convergence of 3 mrad and $C_s = 0.9$ mm. For current C_s -corrected or C_c/C_s -corrected microscopes equipped with field-emission guns, the beam convergence is around 0.1 mrad and C_s is in the order of micrometers. In order to evaluate the influence of high-order terms on the TCCs for the aberration-corrected microscopes operating in the range of 40–80 kV, we calculate the full *mixed coherence function* (MCF):

$$E(\vec{q}_1, \vec{q}_2) = \iint f(\epsilon)s(\vec{\Theta})\exp\{-i[\chi(\vec{q}_1 + k_0\vec{\Theta}, \Delta f + \epsilon) - \chi(\vec{q}_1, \Delta f)]\} \exp\{i[\chi(\vec{q}_2 + k_0\vec{\Theta}, \Delta f + \epsilon) - \chi(\vec{q}_2, \Delta f)]\}d\epsilon d^2\vec{\Theta}. \quad (6)$$

Correspondingly, the TCC $T(\vec{q}_1, \vec{q}_2)$ in (1) can be written as

$$T(\vec{q}_1, \vec{q}_2) = A(\vec{q}_1)A(\vec{q}_2)\exp[-i\chi(\vec{q}_1, \Delta f)]\exp[i\chi(\vec{q}_2, \Delta f)]E(\vec{q}_1, \vec{q}_2). \quad (7)$$

For the calculation of (6), we adopt normalized Gaussian functions for $s(\vec{\Theta})$ and $f(\epsilon)$:

$$s(\vec{\Theta}) = \frac{1}{\pi\Theta_s^2}\exp\left(-\frac{\Theta^2}{\Theta_s^2}\right), \quad (8)$$

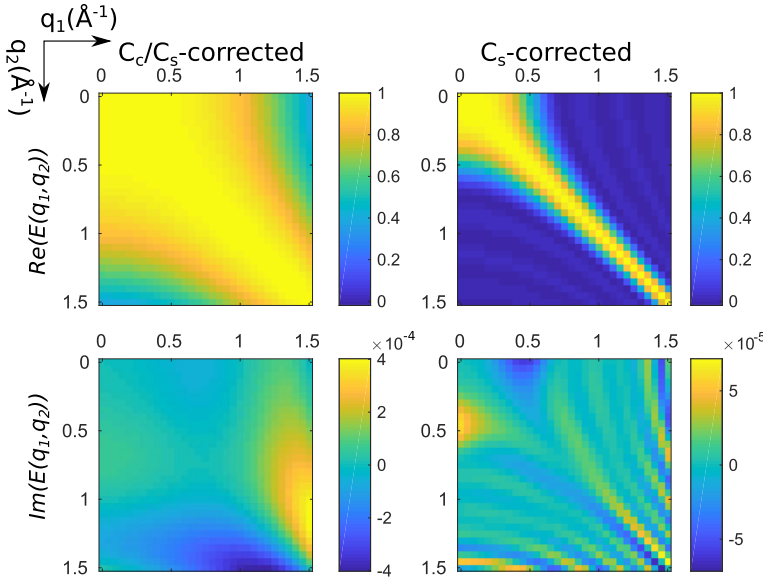


Fig. 1. Real and imaginary parts of the full MCF (6) for a) a C_c/C_s -corrected microscope and b) a C_s -corrected microscope operating at 80 kV. For the evaluation, the convergence of the illumination Θ_s is set to 0.1 mrad; the focal spread is 5 Å for the C_c/C_s -corrected microscope and 4 nm for the C_s -corrected microscope. Other aberration coefficients: $C_s = 4$ mm, $C_3 = -12.3 \mu\text{m}$, $df = 7.6$ nm.

$$f(\epsilon) = \frac{1}{\sigma_c \sqrt{2\pi}} \exp\left(-\frac{\epsilon^2}{2\sigma_c^2}\right), \quad \sigma_c = C_c \frac{\sqrt{\langle(\Delta E)^2\rangle}}{E_0}. \quad (9)$$

Here Θ_s is the characteristic angle of the source emission, and Θ is the semi-angle subtending the direction of the emitted partial wave with the optical axis. For C_s -corrected microscopes, the standard deviation σ_c of the chromatic focal spread depends on the coefficient C_c of the chromatic aberration, the mean quadratic energy spread $\langle(\Delta E)^2\rangle$, and the nominal electron energy E_0 . In this case, the magnitude of σ_c is around several nanometers. For C_c/C_s -corrected microscopes, the residual focal spread is introduced by the instability of the lens current. In this case, σ_c does not depend on C_c and is only several Angstroms.

We calculated $E(\vec{q}_1, \vec{q}_2)$ for a C_c/C_s -corrected microscope and a C_s -corrected microscope operating at 80 kV (Fig. 1). In both cases, the characteristic angle of the source emission Θ_s is set to 0.1 mrad. The parameter σ_c in (9) is set to 5 Å for the C_c/C_s -corrected microscope and 4 nm for the C_s -corrected microscope. As shown in Fig. 1, $E(\vec{q}_1, \vec{q}_2)$ is a complex. Its real part $\text{Re}(E(\vec{q}_1, \vec{q}_2))$ is a symmetric matrix, and its imaginary part $\text{Im}(E(\vec{q}_1, \vec{q}_2))$ is a skew-symmetric matrix.

The image can be calculated by:

$$\begin{aligned} I(\vec{\rho}) &= \iint \tilde{\psi}(\vec{q}_1) \tilde{\psi}^*(\vec{q}_2) A(\vec{q}_1) A(\vec{q}_2) \exp[-i\chi(\vec{q}_1) \\ &\quad + i\chi(\vec{q}_2)] E(\vec{q}_1, \vec{q}_2) e^{i2\pi\vec{\rho} \cdot (\vec{q}_1 - \vec{q}_2)} d^2\vec{q}_1 d^2\vec{q}_2 \\ &= \iint \tilde{\psi}(\vec{q}_1) \tilde{\psi}^*(\vec{q}_2) A(\vec{q}_1) A(\vec{q}_2) \exp[-i\chi(\vec{q}_1) + i\chi(\vec{q}_2)] \\ &\quad [\text{Re}(E(\vec{q}_1, \vec{q}_2)) + i\text{Im}(E(\vec{q}_1, \vec{q}_2))] e^{i2\pi\vec{\rho} \cdot (\vec{q}_1 - \vec{q}_2)} d^2\vec{q}_1 d^2\vec{q}_2. \end{aligned} \quad (10)$$

In our case, the contribution of $\text{Im}(E(\vec{q}_1, \vec{q}_2))$ to the image $I(\vec{\rho})$ is negligible. For a 6 nm thick multi-layered MoTe_2 sample imaged in a C_s -corrected microscope at 80 kV, the numerical evaluation shows that the image intensity associated with $\text{Im}(E(\vec{q}_1, \vec{q}_2))$ is in the order of $O(10^{-14})$. For simplicity, we use $E(\vec{q}_1, \vec{q}_2)$ to represent $\text{Re}(E(\vec{q}_1, \vec{q}_2))$ in the following calculations. Fig. 2 compares the real part of the complex MCF $E(\vec{q}_1, \vec{q}_2)$ calculated from (6) and the first-order MCF [9] for aberration-corrected microscopes operating at 40 kV, 60 kV, and 80 kV. The first-order MCF is the product of the *mixed temporal coherence function* $E_c(\vec{q}_1, \vec{q}_2)$ and the *mixed spatial coherence function* $E_s(\vec{q}_1, \vec{q}_2)$:

$$E(\vec{q}_1, \vec{q}_2) = E_c(\vec{q}_1, \vec{q}_2) E_s(\vec{q}_1, \vec{q}_2), \quad (11)$$

$$E_c(\vec{q}_1, \vec{q}_2) = \exp\left[-\frac{1}{2}(\pi\lambda\sigma_c)^2(q_1^2 - q_2^2)^2\right], \quad (12)$$

$$E_s(\vec{q}_1, \vec{q}_2) = \exp\left[-\left(\frac{\pi\Theta_s}{\lambda}\right)^2(\nabla\chi(\vec{q}_1) - \nabla\chi(\vec{q}_2))^2\right]. \quad (13)$$

The comparison is made in two directions - $(q, 0)$ and $(q, -q)$. $E(q, 0)$ corresponds to the envelope function applied in the quasi-coherent model. For both C_s -corrected microscope (Fig. 2 a) and C_c/C_s -corrected microscope (Fig. 2 b), the first-order MCF [9] and the full MCF calculated from (6) are close. As a short conclusion, the first-order TCC is sufficient for the simulation of aberration-corrected HRTEM images at low voltages in the range of 40–80 kV.

2.2. The quasi-coherent model

In the quasi-coherent model, partial coherence is taken into account by multiplying the wave function at the diffraction plane with the envelope functions. An envelope function is obtained by factorizing the MCF: $E(\vec{q}_1, \vec{q}_2) = E(\vec{q}_1)E(\vec{q}_2)$. This is only possible if the parameters σ_c in (12) and Θ_s in (13) characterizing the partial coherence are small, or the image intensity is mainly contributed by the unscattered waves, e.g. in the case of weak phase objects. By setting either q_1 or q_2 in $E(\vec{q}_1, \vec{q}_2)$ to zero, one obtains the corresponding envelope functions $E(\vec{q}_1)$ applied in the quasi-coherent model. In this case, the transfer function (7) factorizes:

$$T(\vec{q}_1, \vec{q}_2) = T(\vec{q}_1)T(\vec{q}_2), \quad (14)$$

where each factor is given by the transfer function

$$T(\vec{q}) = A(\vec{q}) \exp[-i\chi(\vec{q}, \Delta f)] E_c(\vec{q}) E_s(\vec{q}). \quad (15)$$

By substituting (14) for $T(\vec{q}_1, \vec{q}_2)$ in (2), we readily obtain

$$I(\vec{\rho}) = \left| \iint \tilde{\psi}(\vec{q}) T(\vec{q}) e^{i2\pi\vec{\rho} \cdot \vec{q}} d^2\vec{q} \right|^2. \quad (16)$$

As a final step, the camera MTF is included by applying (5), and $\tilde{I}(\vec{q})$ is acquired by the Fourier transform of the image $I(\vec{\rho})$ in (16).

2.3. Image spread in image simulations

Image spread results from the Johnson noise [21] and is caused by

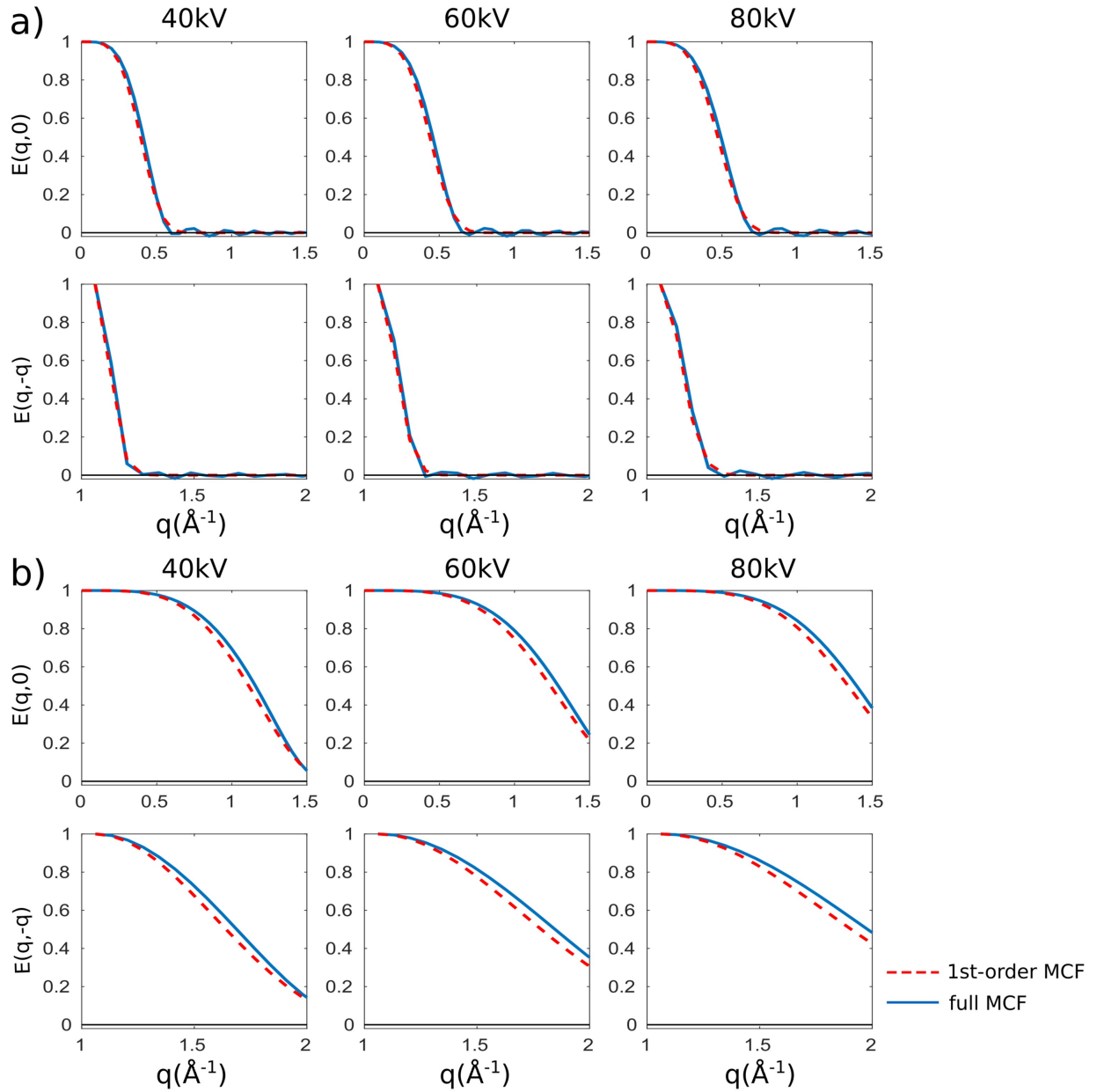


Fig. 2. Comparison of the first-order MCF and the full MCF along two directions - $(q, 0)$ and $(q, -q)$ for a) a C_s -corrected microscope and b) a C_c/C_s -corrected microscope operating at 40 kV, 60 kV and 80 kV. For all accelerating voltages, the 5th-order spherical aberration coefficient C_5 is set to 4 mm. The 3rd-order spherical aberration C_3 and defocus are calculated according to [24]. The convergence of the illumination is set to 0.1 mrad; the focal spread is set to 5 Å for the C_c/C_s -corrected microscope and 4 nm for the C_s -corrected microscope.

thermally induced currents in the lenses and especially in the elements of the C_c/C_s -corrector and the vacuum tube. The image spread is simulated by adding a dipole term in the plane shift. The image intensity is then averaged over all orientations and magnitudes of the dipole, causing a random shift of the image intensity on the detector. The image spread distribution function referred back to the objective plane is given by

$$h(\vec{\rho}_0) = \frac{1}{2\pi\sigma_e^2} \exp\left(-\frac{\rho_0^2}{2\sigma_e^2}\right). \quad (17)$$

The standard deviation σ_e of the Gaussian distribution is voltage-dependent and is in the range of 20 - 30 pm for a C_c/C_s -corrected microscope. In the case of a C_s -corrected microscope, the influence of chromatic aberration dominates, and the effect of image spread is usually negligibly small. The mixed image spread function is calculated by

$$\begin{aligned} E_{im}(\vec{q}_1, \vec{q}_2) &= \int h(\vec{\rho}_0) e^{-i2\pi\vec{\rho}_0 \cdot (\vec{q}_1 - \vec{q}_2)} d^2\vec{\rho}_0 \\ &= \exp\left[-\frac{1}{2}(2\pi\sigma_e)^2(\vec{q}_1 - \vec{q}_2)^2\right]. \end{aligned} \quad (18)$$

The mixed image spread function $E_{im}(\vec{q}_1, \vec{q}_2)$ can be incorporated into the MCF function (11) as [22]:

$$E(\vec{q}_1, \vec{q}_2) = E_c(\vec{q}_1, \vec{q}_2) E_s(\vec{q}_1, \vec{q}_2) E_{im}(\vec{q}_1, \vec{q}_2). \quad (19)$$

By using (4) for image simulation, one notices that $E_{im}(\vec{q}_1, \vec{q}_1 - \vec{q})$ is a function of \vec{q} only. As a result, the incorporation of the term $E_{im}(\vec{q}_1, \vec{q}_1 - \vec{q})$ in (4) is equivalent to multiplying an envelope function $E_{im}(\vec{q})$ with (4). The final image $I_D(\vec{r})$ becomes

$$I_D(\vec{r}) = \int \tilde{I}(\vec{q}) E_{im}(\vec{q}) MTF(\vec{q}) e^{i2\pi\vec{r} \cdot \vec{q}} d^2\vec{q}. \quad (20)$$

Fig. 3 shows the plots of the three envelope functions $E_s(q)$, $E_c(q)$ and

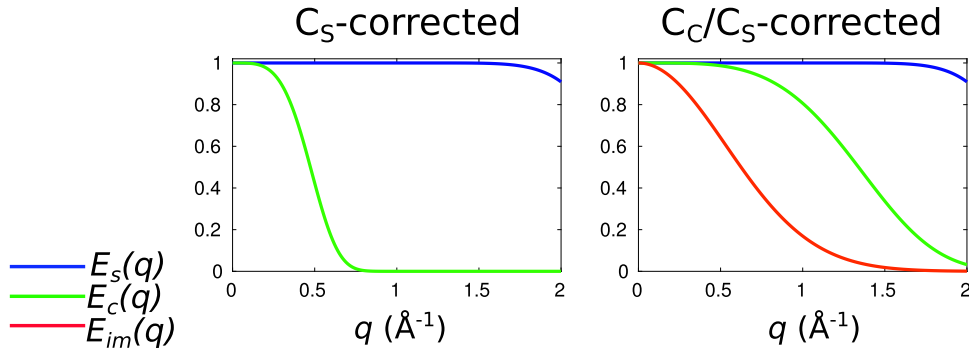


Fig. 3. Plots of $E_s(q)$, $E_c(q)$ and $E_{im}(q)$ for a C_s -corrected ($\sigma_c = 4$ nm, $\sigma_e = 0$) microscope and a C_c/C_s -corrected ($\sigma_c = 5$ Å, $\sigma_e = 30$ pm) microscope operating at 80 kV. The characteristic angle of the source emission is $\Theta_s = 0.1$ mrad for both microscopes.

$E_{im}(q)$ for a C_s -corrected microscope and a C_c/C_s -corrected microscope operating at 80 kV. The functions $E_s(q)$, $E_c(q)$ and $E_{im}(q)$ are obtained by setting either \vec{q}_1 or \vec{q}_2 to zero in (12), (13) and (18). For a C_s -corrected microscope, the temporal envelope removes the contributions from spatial frequencies $\geq 0.7 \text{ Å}^{-1}$. In the case of a C_c/C_s -corrected microscope, the removal of the high-frequency contributions mainly results from the image-spread envelope. For both kinds of microscopes, the spatial envelope plays a minor role on the image contrast.

3. Comparison between experimental and simulated images for monolayered and bilayered MoTe₂

We have compared the experimental HRTEM images with the ones simulated by using the incoherent summation approach ((3) and (20)), the first-order TCC model ((4), (7), (11) and (20)) and the quasi-coherent model ((15), (16) and (20)). In our simulations employing the TCC, no spatial frequency is cut off for improving the computational efficiency. Comparisons have been made for monolayered and bilayered MoTe₂ because of their defined thickness. Monolayered MoTe₂ has been investigated in both the C_s -corrected and the C_c/C_s -corrected microscopes at the accelerating voltage of 80 kV. Bilayered MoTe₂ has been investigated in the C_c/C_s -corrected microscope at 80 kV. The experimental images showing the highest contrast are picked out and normalized. In order to normalize the image, we first apply a Gaussian filter to the raw image with a blurring radius $r = 100\sigma$, where σ is the standard deviation of the Gaussian blur. Subsequently, the normalized image is obtained by dividing the raw experimental image by the Gaussian blurred one. For the simulations we use the experimental microscope parameters listed in Appendix A.

Monolayered MoTe₂ contains three atomic layers and has a thickness of 3.6 Å . The top and bottom layers consist solely of tellurium atoms ($Z = 52$) with a AA stacking order, and the middle layer consists entirely of molybdenum atoms ($Z = 42$). In the case of monolayered MoTe₂ imaged in the C_s -corrected microscope at 80 kV (1st column in Fig. 4), the TCC model and the incoherent summation approach produce the same result, which matches better with the experiment than the quasi-coherent model does (1st line-profile plot in Fig. 4). The discrepancy between the experiment and the simulation using the quasi-coherent model is significantly larger for the higher peak corresponding to the two tellurium atoms in AA stacking order, than for the lower peak corresponding to the molybdenum atom. The peak height is approximately proportional to the sum of the atomic numbers in the corresponding column. The 1st line-profile plot shown in Fig. 4 demonstrates, the larger the sum of the atomic numbers, the larger the error introduced by the quasi-coherent model in the case of the C_s -corrected microscope. For monolayered and bilayered MoTe₂ investigated in the C_c/C_s -corrected microscope at 80 kV, all three models produce similar results comparable to the experiments, demonstrated by the 2nd and 3rd line-profile plots in Fig. 4.

As a summary, the images simulated by using the incoherent summation approach and the TCC model are almost identical for both C_s -corrected and C_c/C_s -corrected microscopes operating at 80 kV. The quasi-coherent model introduces remarkable errors for modelling the imaging of high-Z samples in the C_s -corrected microscope, exemplified by monolayered MoTe₂. However, this model still provides a sufficient approximation for imaging monolayered and bilayered MoTe₂ in the C_c/C_s -corrected microscope. In Section 4 the performance of the quasi-coherent model for the C_s -corrected microscope and for the C_c/C_s -corrected microscope is discussed.

4. Performance of the quasi-coherent model for C_s -corrected and C_c/C_s -corrected microscopes

The example of monolayered MoTe₂ imaged at 80 kV in Fig. 4 shows that compared with the experiments, the error introduced by using the quasi-coherent model is larger for the C_s -corrected microscope than for the C_c/C_s -corrected microscope. The dominant factor leading to the difference between a C_s -corrected and a C_c/C_s -corrected microscope is the chromatic aberration. In the TCC model, chromatic aberration is taken into account by the mixed temporal coherence function $E_c(\vec{q}_1, \vec{q}_2)$ (Eq. (12)). In the quasi-coherent model, chromatic aberration is accounted for by the temporal envelope function $E_c(\vec{q})$. For Gaussian distribution of the focal length caused by the energy spread of the source, the mixed function $E_c(\vec{q}_1, \vec{q}_2)$ is given by

$$\begin{aligned} E_c(\vec{q}_1, \vec{q}_2) &= \exp \left[-\frac{1}{2} (\pi \lambda \sigma_c)^2 (q_1^4 - 2q_1^2 q_2^2 + q_2^4) \right] \\ &= E_c(\vec{q}_1) E_c(\vec{q}_2) \exp [(\pi \lambda \sigma_c)^2 q_1^2 q_2^2]. \end{aligned} \quad (21)$$

The first two functions of the second relation are the temporal envelope functions. The last function $\exp[(\pi \lambda \sigma_c)^2 q_1^2 q_2^2]$ guarantees the conservation of intensity given by $E(\vec{q}_1 = \vec{q}_2) = 1$. This correlation factor is neglected in the quasi-coherent model.

The term σ_c is always positive. In the case of the C_c/C_s -corrected microscope, σ_c is several Angstroms; whereas it is several nanometers for the C_s -corrected microscope. While the envelope functions $E_c(\vec{q}_1)$ and $E_c(\vec{q}_2)$ decrease exponentially, the last factor $\exp[(\pi \lambda \sigma_c)^2 q_1^2 q_2^2]$ increases exponentially, in order to conserve the total intensity. Hence, neglecting this term leads to a removal of image intensity. The loss of image intensity in this case is also interpreted as achromatic interference effect [25].

In the case of the C_s -corrected microscope, more image intensity is cut off by the envelope function $E_c(\vec{q})$ than in the case of the C_c/C_s -corrected microscope, since σ_c is larger in the former case. Without conserving the intensity by keeping the factor $\exp[(\pi \lambda \sigma_c)^2 q_1^2 q_2^2]$, the quasi-coherent model leads to larger errors for the C_s -corrected microscope than for the C_c/C_s -corrected microscope. The following discussions mainly focus on the influence of sample thickness,

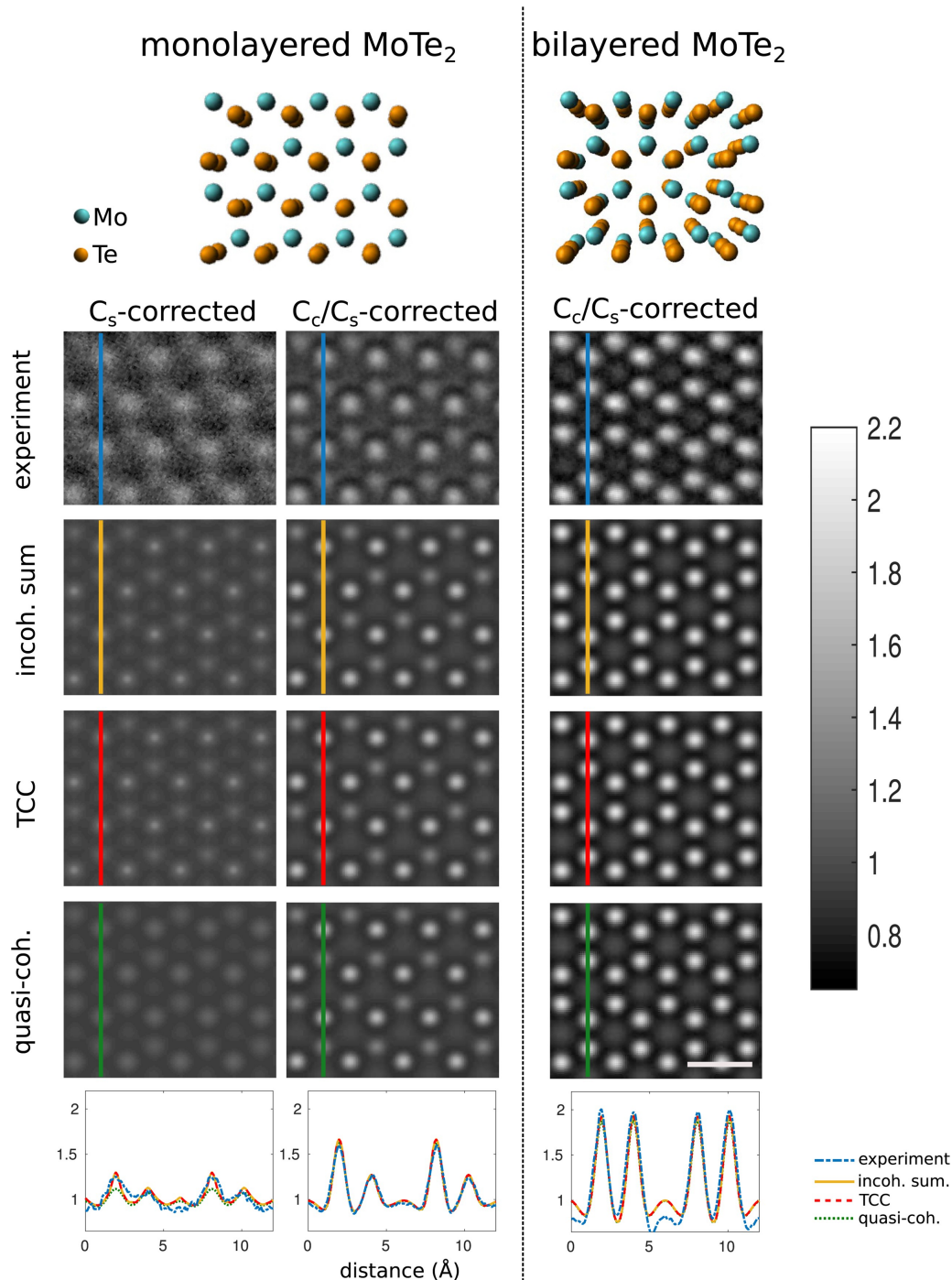


Fig. 4. Comparison between experimental and simulated HRTEM images for monolayered and bilayered MoTe₂ at 80 kV. The 1st and 2nd columns display the images of monolayered MoTe₂ for the C_s -corrected microscope and the C_c/C_s -corrected microscope, respectively. The 3rd column displays the images of the bilayered MoTe₂ for the C_c/C_s -corrected microscope. The two structure models are displayed above. The 1st row shows the experimental images. The 2nd–4th rows show the simulated images using the incoherent summation approach, the TCC model and the quasi-coherent model, respectively. All microscope parameters are the same for the simulations in the same column, and the values are given in [Appendix A](#). The last row displays the line profiles marked in the images from the same column. Scale bar: 5 Å.

atomic number and accelerating voltage on the performance of the quasi-coherent model for the C_s -corrected and C_c/C_s -corrected microscopes.

4.1. Influence of sample thickness

We have simulated the HRTEM images for MoTe₂ of different thicknesses by using the quasi-coherent model, the first-order TCC model and the incoherent summation approach. The simulations are made for both C_s -corrected and C_c/C_s -corrected microscopes operating at 80 kV. The thickness of the MoTe₂ increases from bilayer (1 nm, 6 atomic layers) to twenty layers (14 nm, 60 atomic layers). We compare

the images by calculating the ratios between the highest central intensities of the atom columns: $I_{qc}^{(c)}/I_{incoh}^{(c)}$ and $I_{tcc}^{(c)}/I_{incoh}^{(c)}$. Here I_{qc} , I_{tcc} and I_{incoh} are the images simulated with the quasi-coherent model, the TCC model and the incoherent summation approach, respectively. The ratio $I_{tcc}^{(c)}/I_{incoh}^{(c)}$ is close to 1 for all given sample thicknesses, as well as for both C_s -corrected and C_c/C_s -corrected microscopes, demonstrating that the first-order TCC model and the incoherent summation approach are comparable in our case.

Fig. 5 shows the ratio $I_{qc}^{(c)}/I_{incoh}^{(c)}$ in dependence on the number of atomic layers contained in the MoTe₂ samples for both C_s -corrected and C_c/C_s -corrected microscopes. In both cases, the ratio $I_{qc}^{(c)}/I_{incoh}^{(c)}$ declines as the sample thickness increases. For the C_s -corrected

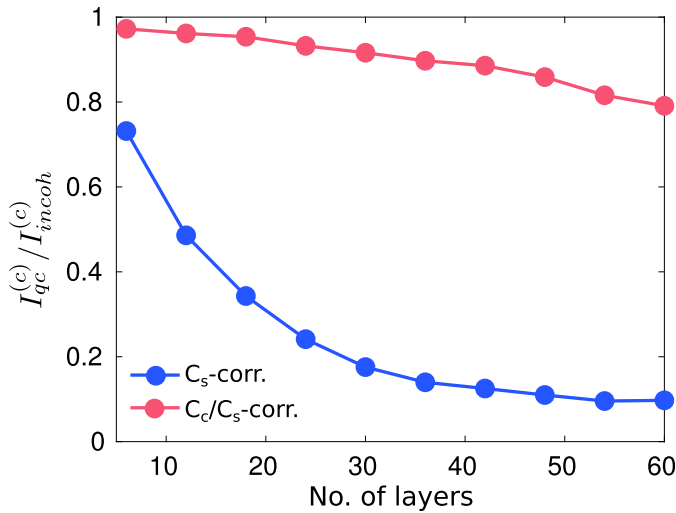


Fig. 5. The ratio between the highest central intensities of the atom columns $I_{qc}^{(c)}/I_{incoh}^{(c)}$ in dependence on the thickness of MoTe₂ quantified by the number of atomic layers. I_{qc} and I_{incoh} are the images simulated by using the quasi-coherent model and the incoherent summation approach, respectively. The blue line and red line correspond to the calculations for the C_s -corrected microscope ($\sigma_c = 4$ nm, $\sigma_e = 0$) and the C_c/C_s -corrected microscope ($\sigma_c = 5$ Å, $\sigma_e = 30$ pm), respectively. All the calculations have assumed an accelerating voltage of 80 kV and a convergent angle of 0.1 mrad for the illumination. Other aberration parameters: $C_s = 2$ mm, $C_s = -7.77$ μ m $df = 6.1$ nm. (For interpretation of the references to colour in this figure legend, the reader is referred to the web version of this article.)

microscope (blue line), $I_{qc}^{(c)}/I_{incoh}^{(c)}$ is below 0.8 for all thicknesses. As the number of atomic layers grows above thirty, corresponding to a thickness of 6.6 nm, the ratio tends to converge towards 0.1. In the case of the C_c/C_s -corrected microscope (red line), the ratio $I_{qc}^{(c)}/I_{incoh}^{(c)}$ is above 0.79 for all thicknesses in the given range and declines approximately linearly with the number of atomic layers. As a short summary, the error introduced by the quasi-coherent model grows as the sample thickness increases, and the error is remarkable for the C_s -corrected microscope.

4.2. Influence of atomic number and accelerating voltage

In order to demonstrate the error introduced by the quasi-coherent model for different atoms and accelerating voltages, we have simulated the images I_{qc} and I_{incoh} of single atoms by using the quasi-coherent model and the incoherent summation approach, respectively (Fig. 6). We have implemented the Wentzel-Yukawa potential for the calculations [26]. The Wentzel-Yukawa potential is sufficient for modelling a single atom if the inner-shell structure of the atom can be neglected. The ratio of the central intensities of the atom images - $I_{qc}^{(c)}/I_{incoh}^{(c)}$ is plotted as a function of atomic number for both C_s -corrected and C_c/C_s -corrected microscopes operating at 40 kV, 60 kV and 80 kV. The focal spread σ_c is set to 4 nm for the C_s -corrected microscope, and 0.5 nm for the C_c/C_s -corrected microscope, respectively. The image spread σ_e is set to 0 for the C_s -corrected microscope and 30 pm for the C_c/C_s -corrected microscope. Usually both the focal spread σ_c and the image spread σ_e vary with the accelerating voltages. However, in order to show solely the influence of voltage on the difference between the two models and minimize the number of variables, we use fixed focal spread values and image spread values for the calculations.

In the case $I_{qc}^{(c)}/I_{incoh}^{(c)} \approx 1$, the quasi-coherent model produces similar result as the incoherent summation approach does. This behavior holds approximately true for all atoms in the range ($Z < 100$) imaged in a

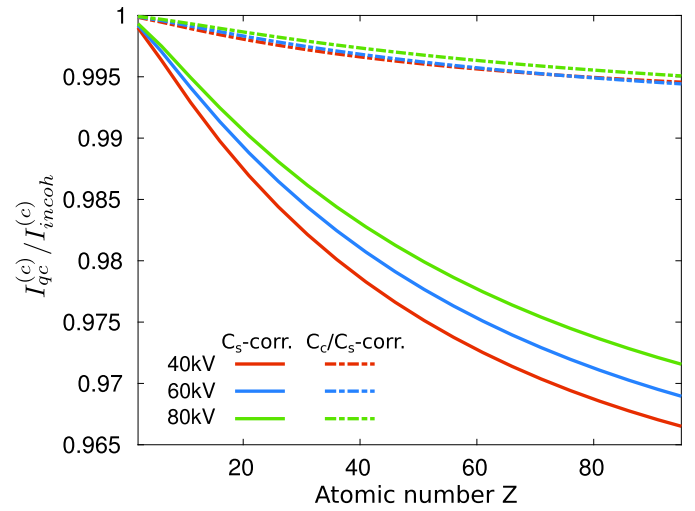


Fig. 6. The ratio between the central intensities of the atom images - $I_{qc}^{(c)}/I_{incoh}^{(c)}$ in dependence of the atomic number Z . I_{qc} and I_{incoh} are the images simulated by using the quasi-coherent model and the incoherent summation approach, respectively. Different colors represent different accelerating voltages: 40 kV (red), 60 kV (blue) and 80 kV (green). The dashed lines represent calculations for the C_c/C_s -corrected microscope ($\sigma_c = 5$ Å, $\sigma_e = 30$ pm), and the solid lines are for the C_s -corrected microscope ($\sigma_c = 4$ nm, $\sigma_e = 0$). All calculations have assumed a convergent angle of 0.1 mrad for the illumination and $C_s = 2$ mm. Defocus and C_s are obtained based on C_s [27]. (For interpretation of the references to colour in this figure legend, the reader is referred to the web version of this article.)

C_c/C_s -corrected microscope operating between 40–80 kV (Fig. 6 dashed lines). For the C_s -corrected microscope, the ratio $I_{qc}^{(c)}/I_{incoh}^{(c)}$ is larger than 0.99 for atoms with $Z \leq 20$ at 80 kV (Fig. 6 green solid line) and $Z \leq 16$ at 40 kV (Fig. 6 red solid line). Under these conditions, the quasi-coherent model still provides a sufficient approximation. The ratio $I_{qc}^{(c)}/I_{incoh}^{(c)}$ decreases when the acceleration voltage declines in the case of the C_s -corrected microscope, which is consistent with the conclusion drawn from (21). Since decreasing the accelerating voltage increases the wavelength λ in (21), the disregard of the factor $\exp[(\pi\lambda\sigma_c)^2 q_1^2 q_2^2]$ in the quasi-coherent model leads to notable errors if both σ_c and λ are large.

5. Summary

We have applied the incoherent summation approach, the first-order TCC model and the quasi-coherent model in HRTEM image simulations for aberration-corrected low-voltage microscopes operating in the range between 40–80 kV. Based on the comparison between the simulations and the experiments for monolayered and bilayered MoTe₂ imaged at 80 kV, the incoherent summation approach and the TCC model match the experiments for both C_s -corrected and C_c/C_s -corrected microscopes. The quasi-coherent model provides a sufficient approximation for simulating the imaging of low- Z materials in a C_s -corrected microscope and the imaging of high- Z samples in a C_c/C_s -corrected microscope, as long as the samples contain only several atomic layers. However, this model introduces appreciable errors for modelling the imaging of high- Z materials in a C_s -corrected microscope. The errors become larger when the atomic number or the sample thickness increases, as well as when the accelerating voltage decreases. For aberration-corrected microscopes operating at 40–80 kV, the first-order TCC model and the incoherent summation approach always serve as reliable options for HRTEM image simulations.

Acknowledgment

We thank Janis Köster for successfully achieving the challenge of preparing the MoTe₂ sample and gratefully acknowledge financial

support by the DFG (German Research Foundation) and the Ministry of Science, Research and the Arts (MWK) of Baden-Württemberg in the frame of the (Sub-Angstrom Low-Voltage Electron microscopy) (SALVE) project.

Appendix A. Experimental and computational details

Monolayered and bilayered MoTe₂ samples were prepared with the exfoliation method and transferred to TEM grids [28]. The thickness of the layers were estimated from contrast measurements [29,30]. HRTEM imaging has been performed by using the C_s-corrected FEI Titan 80–300 and the C_c/C_s-corrected SALVE instrument, both operating at 80 kV. Focal series were recorded on the GIF camera with a fine sampling around 0.1 Å/pixel. The camera MTF has been applied in the image simulations and its influence on the image contrast is negligible. Subsequently, the optimum image is picked out based on the contrast evaluation [31].

The calculations in Fig. 4 have employed Wentzel–Yukawa potential [26] with the Debye–Waller factor incorporated. We have used a Debye–Waller factor of 0.58 Å² for MoTe₂, estimated based on the mean square relative displacement $\langle u^2 \rangle = 74 \text{ pm}^2$ of the bonds Mo–Mo and Te–Te [32] by using the relation $B = 8\pi^2 \langle u^2 \rangle$ [33].

Experimental microscope parameters implemented in the calculations are listed in Table A1.

Table A1

Microscope parameters applied for the imaging of mono- and bi-layered MoTe₂. Here σ_c represents the focal spread, σ_i denotes the image spread; θ_s is divergence of the illumination; C₅ and C_s are the coefficients of the 5th-order and 3rd-order spherical aberration, respectively.

Type	Sample	σ_c (nm)	σ_i (pm)	θ_s (mrad)	C ₅ (mm)	C _s (μm)	Δf (Å)
SALVE	MoTe ₂ (1 layer)	0.5	30	0.1	1.994	−7.757	61
	MoTe ₂ (2 layers)				2.114	−8.06	64
Titan	MoTe ₂ (1 layer)	4	0	0.1	0	−3	38

References

- [1] H. Rose, Nonstandard imaging methods in electron microscopy, *Ultramicroscopy* 2 (0) (1976) 251–267.
- [2] H. Rose, Information transfer in transmission electron microscopy, *Ultramicroscopy* 15 (1984) 173–191.
- [3] L. Chang, R. Meyer, A. Kirkland, Calculations of HREM image intensity using Monte Carlo integration, *Ultramicroscopy* 104 (3–4) (2005) 271–280.
- [4] B. Forbes, A. d'Alfonso, S. Findlay, D. Van Dyck, J. LeBeau, S. Stemmer, L. Allen, Thermal diffuse scattering in transmission electron microscopy, *Ultramicroscopy* 111 (12) (2011) 1670–1680.
- [5] F.F. Krause, K. Müller, D. Zillmann, J. Jansen, M. Schowalter, A. Rosenauer, Comparison of intensity and absolute contrast of simulated and experimental high-resolution transmission electron microscopy images for different multislice simulation methods, *Ultramicroscopy* 134 (2013) 94–101.
- [6] C. Koch, QSTEM: quantitative TEM/STEM simulations, 2010. https://www.physics.hu-berlin.de/en/sem/software/software_qstem.
- [7] A. Rosenauer, M. Schowalter, STEMSIM—a new software tool for simulation of STEM HAADF Z-contrast imaging, *Microscopy of Semiconducting Materials 2007*, Springer, 2008, pp. 170–172.
- [8] R.H. Wade, J. Frank, Electron microscope transfer functions for partially coherent axial illumination and chromatic defocus spread, *Optik* 49 (1977) 81.
- [9] K. Ishizuka, Contrast transfer of crystal images in TEM, *Ultramicroscopy* 5 (1980) 55–65.
- [10] H. Pulvermacher, Transmission cross-coefficient for electron microscopic imaging with partially coherent illumination and electric instability, *Optik* 60 (1981) 45.
- [11] J.E. Bonevich, L.D. Marks, Contrast transfer theory for non-linear imaging, *Ultramicroscopy* 26 (1988) 313–319.
- [12] K. Ishizuka, xHREM: HREM simulation suite. <https://www.hremresearch.com/Eng/simulation.html>.
- [13] P. Stadelmann, JEMS-EMS java version. <https://www.jems-saas.ch/>.
- [14] J. Barthel, Dr. Probe: a software for high-resolution STEM image simulation, *Ultramicroscopy* 193 (2018) 1–11.
- [15] J. Frank, The envelope of electron microscopic transfer functions for partially coherent illumination, *Optik* 38 (1973) 519.
- [16] W.O. Saxton, Spatial coherence in axial high resolution conventional electron microscopy, *Optik* 49 (1977) 51.
- [17] E.J. Kirkland, *Advanced Computing Electron Microscopy*, Plenum Pr., 1998.
- [18] A. Chuvilil, U. Kaiser, On the peculiarities of CBED pattern formation revealed by multislice simulation, *Ultramicroscopy* 104 (1) (2005) 73–82.
- [19] M. O'Keefe, P. Buseck, Computation of high resolution TEM images of minerals, *Trans. A.C.A.* 15 (1979) 27–46.
- [20] M. Linck, P. Hartel, S. Uhlemann, F. Kahl, H. Müller, J. Zach, M. Haider, M. Niestadt, M. Bischoff, J. Biskupek, et al., Chromatic aberration correction for atomic resolution TEM imaging from 20 to 80 kV, *Phys. Rev. Lett.* 117 (7) (2016) 076101.
- [21] S. Uhlemann, H. Müller, P. Hartel, J. Zach, M. Haider, Thermal magnetic field noise limits resolution in transmission electron microscopy, *Phys. Rev. Lett.* 111 (4) (2013) 046101.
- [22] M. Haider, P. Hartel, H. Müller, S. Uhlemann, J. Zach, Information transfer in a TEM corrected for spherical and chromatic aberration, *Microsc. Microanal.* 16 (04) (2010) 393–408.
- [23] A. Thust, High-resolution transmission electron microscopy on an absolute contrast scale, *Phys. Rev. Lett.* 9 (2009) 220810.
- [24] M. Lentzen, B. Jahnke, C.L. Jia, A. Thust, K. Tillmann, K. Urban, High-resolution imaging with an aberration-corrected transmission electron microscope, *Ultramicroscopy* 92 (2002) 233–242.
- [25] W.M.J. Coene, A. Thust, M.O. de Beeck, D.V. Dyck, Maximum-likelihood method for focus-variation image reconstruction in high resolution transmission electron microscopy, *Ultramicroscopy* 64 (1996) 109–135.
- [26] G. Wentzel, Zwei Bemerkungen über die Zerstreuung korpuskularer Strahlen als Beugungerscheinung, *Zeitschrift für Physik A Hadrons and Nuclei* 40 (8) (1926) 590–593.
- [27] M. Lentzen, Contrast transfer and resolution limits for sub-angstrom high-resolution transmission electron microscopy, *Microsc. Microanal.* 14 (1) (2008) 16–26.
- [28] J.C. Meyer, C. Girit, M. Crommie, A. Zettl, Hydrocarbon lithography on graphene membranes, *Appl. Phys. Lett.* 92 (12) (2008) 123110.
- [29] P. Blake, E. Hill, A. Castro Neto, K. Novoselov, D. Jiang, R. Yang, T. Booth, A. Geim, Making graphene visible, *Appl. Phys. Lett.* 91 (6) (2007) 063124.
- [30] M. Benameur, B. Radisavljevic, J. Heron, S. Sahoo, H. Berger, A. Kis, Visibility of dichalcogenide nanolayers, *Nanotechnology* 22 (12) (2011) 125706.
- [31] Z. Lee, J. Meyer, H. Rose, U. Kaiser, Optimum HRTEM image contrast at 20 kV and 80 kV—exemplified by graphene, *Ultramicroscopy* 112 (1) (2012) 39–46.
- [32] S. Caramazza, C. Marini, L. Simonelli, P. Dore, P. Postorino, Temperature dependent EXAFS study on transition metal dichalcogenides MoX₂ (X = S, Se, Te), *J. Phys.* 28 (32) (2016) 325401.
- [33] L.-M. Peng, G. Ren, S. Dudarev, M. Whelan, Debye–Waller factors and absorptive scattering factors of elemental crystals, *Acta Crystallogr. Sect. A* 52 (3) (1996) 456–470.